

# SPRITE : A New Sparse Approach for 3D High Resolution RCS Imaging

Thomas Benoudiba-Campanini  
*CEA CESTA DAM*  
F-33114 Le Barp, France  
thomas.benoudiba-campanini@cea.fr

Pierre Minvielle  
*CEA CESTA DAM*  
F-33114 Le Barp, France  
pierre.minvielle@cea.fr

Jean-François Giovannelli  
*IMS, Univ. Bordeaux, CNRS, BINP*  
F-33400 Talence, France  
jean-francois.giovannelli@u-bordeaux.fr

Pierre Massaloux  
*CEA CESTA DAM*  
F-33114 Le Barp, France  
pierre.massaloux@cea.fr

**Abstract**—The Radar Cross Section (RCS) characterizes the scattering power of a target exposed to an electromagnetic field. Its analysis and its control are important in many applications. 3D imaging is a suitable tool to accurately locate and characterize in 3D the main contributors to the RCS. However, this is a non-invertible Fourier synthesis problem because the number of unknowns is larger than the number of data. Conventional methods such as the Polar Format Algorithm (PFA), which consists of data reformatting including zero-padding followed by an inverse fast Fourier transform, provide results of limited quality. In this paper, we propose an original new high resolution method, named SPRITE (for SParse Radar Imaging TEchnique), which considerably enhances the resolution of the estimated RCS maps. It is based on a regularization scheme that accounts for information of sparsity and support. The solution is then defined as the minimizer of a penalized and constrained criterion. Optimization is ensured by an adaptation of the ADMM (Alternating Direction Method of Multiplier) that is able to quickly perform calculations using fast Fourier transforms. Finally, the method is evaluated on real data. Compared to the PFA, the resolution is significantly increased, leading to a better RCS analysis and control.

**Index Terms**—SPRITE, HR 3D Imaging, RCS, Inverse Problem, Sparse Regularization, ADMM

## I. INTRODUCTION

Radar Cross Section (RCS) analysis is the characterization of the scattering behavior of a target. It is of great importance when the aim is to reduce the radar target signature (e.g. stealthy targets) or conversely, when the objective is to enhance its signature (e.g. corner reflectors). Three-dimensional (3D) imaging is a common and suitable tool for RCS analysis and control. It consists in mapping the spatial distribution of the target's scatterers from measurements of its backscattered electric field. It started in the late 1970's with one-dimensional (1D) backscattering profiles and two-dimensional (2D) backscattering maps [1]. More recent publications examine 3D backscattering maps [2].

In this paper we propose a new method named SPRITE (for SParse Radar Imaging TEchnique) for 3D RCS imaging. It is applied to real measurement data. It is based on a regularization approach resting on a sparsity promoting criterion with a support constraint. The criterion is then minimized by an Alternating Direction Method of Multipliers (ADMM). The resolution of the 3D RCS maps is drastically enhanced.

The paper is organized as follows. In section II the data acquisition process is presented and the forward model is introduced. Section III is dedicated to the SPRITE method where the estimated map is defined as the solution of an optimization problem. In section IV experimental results for real measurements data are presented and discussed. Finally, section V concludes this paper.

## II. PROBLEM STATEMENT

### A. Data acquisition

Usually, RCS measurements are made by a monostatic radar inside an indoor anechoic chamber facility in order to reduce spurious echoes. As shown in Fig. 1, for any given wave vector  $\mathbf{k}$  the target is illuminated by a far field quasi-planar monochromatic electromagnetic (EM) continuous wave. Each wave vector is linked to a frequency  $f$ , a roll angle  $\varphi$  and an elevation angle  $\theta$  (obtained by rotating both antenna and target) by the following formula:

$$\mathbf{k} = -\frac{2\pi f}{c} \begin{bmatrix} \sin(\theta) \cos(\varphi) \\ \sin(\theta) \sin(\varphi) \\ \cos(\theta) \end{bmatrix} \quad (1)$$

where  $c$  is the light speed.

After a calibration step, a complex scattering coefficient  $\sigma$  is measured. It describes the object-wave interaction (with both amplitude and phase) and it is directly linked to the RCS:

$$\sigma = 2\sqrt{\pi}R \frac{E^S}{E^I}; \quad \text{RCS} = |\sigma|^2 \quad (2)$$

where  $E^I$  and  $E^S$  are respectively the scattered electric field complex amplitude at the radar and the incident electric field complex amplitude at the target and  $R$  is the

radar-target distance. These measurements are repeated for  $M$  different triplets  $(f^{[m]}, \varphi^{[m]}, \theta^{[m]})$ ,  $m = 0, \dots, M - 1$ . Finally, a sequence of  $M$  complex scattering coefficients  $\{\sigma^{[0]}, \sigma^{[1]}, \dots, \sigma^{[M-1]}\}$  is collected.

Let us emphasize that we consider a "small angle small bandwidth" context [3] where the excursions of  $\hat{k}$  are small around a central wave vector of interest  $\hat{k}_c$ .

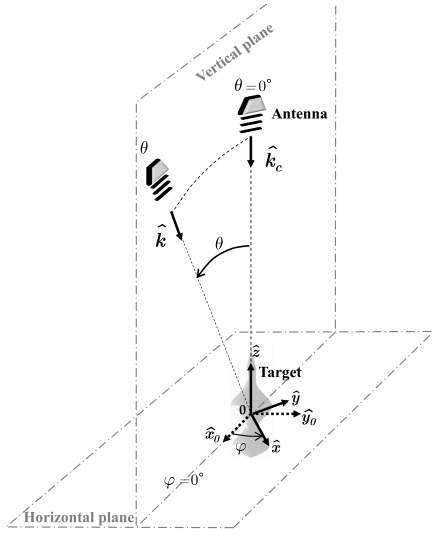


Figure 1: Data acquisition schema.

### B. Forward model

The classical forward model derives from optical physics and stationary-phase method in high frequency [4]. It is written

$$\sigma(\mathbf{k}) = \iiint_{\mathcal{D}} a(\mathbf{r}) \exp\{-2j\pi \mathbf{k} \cdot \mathbf{r}\} d\mathbf{r}, \quad (3)$$

where  $a$  is the spatial EM scattering density,  $\mathbf{r}$  is the spatial position vector and  $\mathcal{D}$  is the radar field-of-view. Note that this model leaves out various physical phenomena such as multiple scattering, creeping waves and shadowing. Yet, it is extensively used because it makes the imaging problem linear, at the cost of possible artifacts [5].

The field-of-view is then divided into  $N$  voxels leading to the following discretized linear observation model:

$$\boldsymbol{\sigma} = \mathbf{H}\mathbf{a} + \mathbf{n} \quad (4)$$

where  $\boldsymbol{\sigma}$  is the observation vector,  $\mathbf{a}$  the vectorized scattering map,  $\mathbf{n}$  a noise vector and  $\mathbf{H}$  the model matrix. If the observations lie on a regular cartesian grid in the  $\mathbf{k}$ -space, after a regridding process for example, it can be shown [6] that  $\mathbf{H}$  can be expressed as follows:

$$\mathbf{H} = \alpha\sqrt{N} \Delta_\Psi \mathbf{S} \mathbf{F} \Delta_\Phi \quad (5)$$

where  $\alpha$  is a complex coefficient accounting for the origin of the spatial and the  $\mathbf{k}$ -space grids,  $\mathbf{S}$  is a 0/1 - binary selection (or sampling) matrix ( $\mathbf{S}$  discards unobserved spatial frequencies),  $\mathbf{F}$  is an unitary 3D discrete Fourier transform matrix,  $\Delta_\Psi$  and  $\Delta_\Phi$  are diagonal phase shifting matrices respectively in the spatial domain and in the  $\mathbf{k}$ -space.

### C. Inverse problem and state of the art

The objective is to determine the scattering map  $\mathbf{a}$  from the observation vector  $\boldsymbol{\sigma}$ : the RCS imaging problem is an inverse problem [7]. Nevertheless,  $\mathbf{H}$  is rank deficient and not invertible because there are more unknowns (voxels to estimate) than data. In order to find a solution, it is mandatory to regularize the problem that means consider prior information on the scattering map  $\mathbf{a}$ .

The Polar Format Algorithm (PFA) [1], [3], [8] is an extensively used technique. It benefits from the polar nature of the frequency-domain acquisition. In far-field, the processing is reduced to a Fourier synthesis problem carried out by an Inverse Fast Fourier Transform (IFFT). [8] exhibits that PFA is exactly the minimum-norm least-squares solution when the observations are on a regular cartesian grid. Nevertheless, it is known that the resolution of the produced images is limited by the frequency bandwidth for the range resolution and by the angular diversity of observations and the wavelength for the cross-range resolution [1]. Moreover, according to the Fourier theory, the finite bandwidth of the radar leads to a particular point spread function: a cardinal sine defocusing function around the scattering centers. This is particularly problematic in a RCS analysis and control context because weak scatterers may be hidden by high sidelobe level. Many methods, mainly based on a spectral weighting called apodization, have been studied to enhance the Peak to SideLobe Ratio (PSLR). However, even if the PSLR is significantly improved, the main lobe beamwidth is increased at the same time, leading to a degraded resolution.

More recently, various publications [9]–[12] have proposed sparse regularization methods for RCS imaging. They rest on the minimization of a criterion with a least square term and a sparse promoting penalty such as the  $\ell_1$  norm of the map. The results produced by these methods are very similar to the one obtained with greedy algorithms such as CLEAN [13] or Orthogonal Matching Pursuit methods [12] and spectral estimation methods such as ESPRIT [14] and MUSIC [15]. The estimated map is made up of scattering points. And yet, it is well known that in a high frequency context, specular reflections are the main scattering mechanisms [16]. Thus, the 3D map should not only be composed of scattering points but also of scattering segments and flat surfaces also called specular facets [17].

## III. SPRITE: THE PROPOSED METHOD

### A. Priors and proposed solution

In order to both increase the resolution and to take into account the available information regarding the wave-target interactions, we consider the five following priors. Each prior is then expressed through a penalty in order to form a criterion.

<b>P1</b>	The projection of $\mathbf{a}$ onto the $\hat{z}$ axis (chosen co-linear to $\hat{k}_c$ , see Fig. 1) is sparse. The associated penalty is $\ \mathbf{P}\mathbf{a}\ _1$ where $\mathbf{P}$ is a projection matrix onto $\hat{z}$ .
-----------	--

<b>P2</b>	The specular facets are connected (in a topological sense) and the scattering coefficient is constant all over each facet. The associated penalties are $\ \mathbf{D}_x \mathbf{a}\ _1$ and $\ \mathbf{D}_y \mathbf{a}\ _1$ where $\mathbf{D}_x$ (resp. $\mathbf{D}_y$ ) is the pixel-wise difference matrix along the $\hat{\mathbf{x}}$ axis (resp. the $\hat{\mathbf{y}}$ axis). Note that these penalties are anisotropic total variation along the $\hat{\mathbf{x}}$ and $\hat{\mathbf{y}}$ axis.
<b>P3</b>	The map energy is low (and in particular for stealthy targets). The penalty term writes $\ \mathbf{a}\ _2^2$ . It also ensures the strict convexity of the further criterion.
<b>P5</b>	The EM extent of the target lies in a finite spatial support. We can consider spatial support constraints $\mathcal{C}$ .

Let us introduce the following criterion:

$$\begin{aligned} \mathcal{J}(\mathbf{a}) = & \frac{1}{2} \|\boldsymbol{\sigma} - \mathbf{H}\mathbf{a}\|_2^2 + \mu \|\mathbf{P}\mathbf{a}\|_1 + \lambda \|\mathbf{D}_x \mathbf{a}\|_1 \\ & + \nu \|\mathbf{D}_y \mathbf{a}\|_1 + \frac{\nu}{2} \|\mathbf{a}\|_2^2 \end{aligned} \quad (6)$$

where  $\|\boldsymbol{\sigma} - \mathbf{H}\mathbf{a}\|_2^2$  is the data fitting term and  $\mu$ ,  $\lambda$  and  $\nu$  are positive regularization parameters. Finally, the estimated map  $\hat{\mathbf{a}}$  is defined as the solution of the following optimization problem

$$\hat{\mathbf{a}} = \operatorname{argmin}_{\mathbf{a} \in \mathbb{C}^N} \left\{ \begin{array}{l} \mathcal{J}(\mathbf{a}) \\ \text{s.t. } \mathbf{a} \in \mathcal{C} \end{array} \right. \quad (7)$$

where  $\mathcal{C}$  is a constraint set [18]. Note that this 3D high-dimensional optimization problem (7) is difficult because the criterion (6) is not differentiable due to  $\ell_1$  norms.

### B. Optimization

The literature devoted to non-differentiable criterion minimization is very vast. For instance we can cite:  $\ell_1$  smoothing methods [19] (eg. the  $\ell_1$  norm is replaced by a differentiable Huber function), subgradient methods [20], proximal gradient methods such as the Forward Backward Splitting [21] with its accelerated version the Fast Iterative Thresholding Algorithm [22] and primal-dual methods such as the dual ascent method, the method of Lagrange multipliers and the Alternating Direction Method of Multipliers (ADMM).

ADMM belongs to the convex optimization algorithms class. It is based on an augmented Lagrangian approach and it is very suitable to find the constrained solution (7). Moreover, in our case, the convergence is guaranteed [23] because  $\mathcal{J}(\mathbf{a})$  is strictly convex for  $\nu > 0$ . In ADMM form, (7) becomes

$$\hat{\mathbf{a}} = \operatorname{argmin}_{\mathbf{a}, \mathbf{v}} \left\{ \begin{array}{l} \mathcal{K}(\mathbf{a}, \mathbf{v}) \\ \text{s.t. } \begin{cases} \mathbf{v}_P = \mathbf{P}\mathbf{a} \\ \mathbf{v}_x = \mathbf{D}_x \mathbf{a} \\ \mathbf{v}_y = \mathbf{D}_y \mathbf{a} \\ \mathbf{v}_C = \mathbf{a} \end{cases} \end{array} \right. \quad (8)$$

with  $\mathbf{v} = [\mathbf{v}_P, \mathbf{v}_x, \mathbf{v}_y, \mathbf{v}_C]$  the vector of auxiliary variables,

$$\begin{aligned} \mathcal{K}(\mathbf{a}, \mathbf{v}) = & \frac{1}{2} \|\boldsymbol{\sigma} - \mathbf{H}\mathbf{a}\|_2^2 + \mu \|\mathbf{v}_P\|_1 + \lambda \|\mathbf{v}_x\|_1 + \lambda \|\mathbf{v}_y\|_1 \\ & + \frac{\nu}{2} \|\mathbf{a}\|_2^2 + \mathcal{I}_C(\mathbf{v}_C) \end{aligned}$$

and  $\mathcal{I}_C$  the characteristic function of the constraint set  $\mathcal{C}$ . Note that the optimal solutions of (7) and (8) are strictly equal.

As  $\mathbf{a} \in \mathbb{C}^N$ , the scaled augmented Lagragian [24] is used:

$$\begin{aligned} \mathcal{L}_\rho(\mathbf{a}, \mathbf{v}, \mathbf{u}) = & \mathcal{K}(\mathbf{a}, \mathbf{v}) + \frac{\rho_P}{2} \left( \|\mathbf{P}\mathbf{a} - \mathbf{v}_P + \mathbf{u}_P\|_2^2 - \|\mathbf{u}_P\|_2^2 \right) \\ & + \frac{\rho_D}{2} \left( \|\mathbf{D}_x \mathbf{a} - \mathbf{v}_x + \mathbf{u}_x\|_2^2 - \|\mathbf{u}_x\|_2^2 + \|\mathbf{D}_y \mathbf{a} - \mathbf{v}_y + \mathbf{u}_y\|_2^2 \right. \\ & \left. - \|\mathbf{u}_y\|_2^2 \right) + \frac{\rho_C}{2} \left( \|\mathbf{a} - \mathbf{v}_C + \mathbf{u}_C\|_2^2 - \|\mathbf{u}_C\|_2^2 \right) \end{aligned} \quad (9)$$

where  $\mathbf{u} = [\mathbf{u}_P, \mathbf{u}_x, \mathbf{u}_y, \mathbf{u}_C]$  is the vector of the scaled Lagrange multipliers and  $\rho = [\rho_P, \rho_D, \rho_C]$  the vector of the strictly positive penalty parameters. Note that (9) is quadratic, strictly convex and differentiable with respect to  $\mathbf{a}$ . Finally, the ADMM algorithm is given by

**Initialize**  $\mathbf{v}^{(0)}$ ,  $\mathbf{u}^{(0)}$  and  $k = 0$ .

**Repeat until convergence**

$$\begin{aligned} \mathbf{a}^{(k+1)} &= \operatorname{argmin}_{\mathbf{a}} \mathcal{L}_\rho(\mathbf{a}, \mathbf{v}^{(k)}, \mathbf{u}^{(k)}) \\ \mathbf{v}_P^{(k+1)} &= \operatorname{argmin}_{\mathbf{v}_P} \mathcal{L}_\rho(\mathbf{a}^{(k+1)}, \mathbf{v}_P, \mathbf{v}_x^{(k)}, \mathbf{v}_y^{(k)}, \mathbf{v}_C^{(k)}, \mathbf{u}^{(k)}) \\ \mathbf{v}_x^{(k+1)} &= \operatorname{argmin}_{\mathbf{v}_x} \mathcal{L}_\rho(\mathbf{a}^{(k+1)}, \mathbf{v}_P^{(k+1)}, \mathbf{v}_x, \mathbf{v}_y^{(k)}, \mathbf{v}_C^{(k)}, \mathbf{u}^{(k)}) \\ \mathbf{v}_y^{(k+1)} &= \operatorname{argmin}_{\mathbf{v}_y} \mathcal{L}_\rho(\mathbf{a}^{(k+1)}, \mathbf{v}_P^{(k+1)}, \mathbf{v}_x^{(k+1)}, \mathbf{v}_y, \mathbf{v}_C^{(k)}, \mathbf{u}^{(k)}) \\ \mathbf{v}_C^{(k+1)} &= \operatorname{argmin}_{\mathbf{v}_C} \mathcal{L}_\rho(\mathbf{a}^{(k+1)}, \mathbf{v}_P^{(k+1)}, \mathbf{v}_x^{(k+1)}, \mathbf{v}_y^{(k+1)}, \mathbf{v}_C, \mathbf{u}^{(k)}) \\ \mathbf{u}_P^{(k+1)} &= \mathbf{u}_P^{(k)} + \mathbf{P}\mathbf{a}^{(k+1)} - \mathbf{v}_P^{(k+1)} \\ \mathbf{u}_x^{(k+1)} &= \mathbf{u}_x^{(k)} + \mathbf{D}_x \mathbf{a}^{(k+1)} - \mathbf{v}_x^{(k+1)} \\ \mathbf{u}_y^{(k+1)} &= \mathbf{u}_y^{(k)} + \mathbf{D}_y \mathbf{a}^{(k+1)} - \mathbf{v}_y^{(k+1)} \\ \mathbf{u}_C^{(k+1)} &= \mathbf{u}_C^{(k)} + \mathbf{a}^{(k+1)} - \mathbf{v}_C^{(k+1)} \\ k &= k + 1 \end{aligned}$$

Note that the updates of the auxiliary variables can be written

$$\begin{aligned} \mathbf{v}_P^{(k+1)} &= \mathbf{S}_{\mu/\rho_P}(\mathbf{P}\mathbf{a}^{(k+1)} + \mathbf{u}_P^{(k)}) \\ \mathbf{v}_x^{(k+1)} &= \mathbf{S}_{\lambda/\rho_D}(\mathbf{D}_x \mathbf{a}^{(k+1)} + \mathbf{u}_x^{(k)}) \\ \mathbf{v}_y^{(k+1)} &= \mathbf{S}_{\lambda/\rho_D}(\mathbf{D}_y \mathbf{a}^{(k+1)} + \mathbf{u}_y^{(k)}) \\ \mathbf{v}_C^{(k+1)} &= \mathcal{P}_C(\mathbf{a}^{(k+1)} + \mathbf{u}_C^{(k)}) \end{aligned} \quad (10)$$

with  $\mathbf{S}$  the soft thresholding operator for complex variables [24] and  $\mathcal{P}_C$  the Euclidean projection onto  $\mathcal{C}$ . Let us emphasize that the  $\mathbf{v}$  and  $\mathbf{u}$  updates are direct and separable.

The  $\mathbf{a}$ -update is obtained by nullifying the gradient of (9) and finally

$$\mathbf{a}^{(k+1)} = \mathbf{G}^{-1} \mathbf{d}^{(k)} \quad (11)$$

where  $\mathbf{G} = \mathbf{H}^\dagger \mathbf{H} + \rho_P \mathbf{P}^\dagger \mathbf{P} + \rho_D (\mathbf{D}_x^\dagger \mathbf{D}_x + \mathbf{D}_y^\dagger \mathbf{D}_y) + (\nu + \rho_C) \mathbf{I}_N$

$$\begin{aligned} \mathbf{d}^{(k)} &= \mathbf{H}^\dagger \boldsymbol{\sigma} + \mathbf{t}^{(k)} \\ \mathbf{t}^{(k)} &= \rho_P \mathbf{P}^\dagger (\mathbf{v}_P^{(k)} - \mathbf{u}_P^{(k)}) + \rho_D [\mathbf{D}_x^\dagger (\mathbf{v}_x^{(k)} - \mathbf{u}_x^{(k)}) \\ & \quad + \mathbf{D}_y^\dagger (\mathbf{v}_y^{(k)} - \mathbf{u}_y^{(k)})] + \rho_C (\mathbf{v}_C^{(k)} - \mathbf{u}_C^{(k)}) \end{aligned}$$

and  $\mathbf{H}^\dagger$  is the Hermitian transpose of  $\mathbf{H}$ . It must be noted that  $\mathbf{P}^\dagger \mathbf{P}$ ,  $\mathbf{D}_x^\dagger \mathbf{D}_x$ ,  $\mathbf{D}_y^\dagger \mathbf{D}_y$ ,  $\mathbf{I}_N$  and from (5)  $\mathbf{H}^\dagger \mathbf{H}$  are 3-level circulant matrices. Thus,  $\mathbf{G}$  is also a 3-level circulant matrix which can be diagonalized in the Fourier domain:  $\mathbf{G} = \mathbf{F}^\dagger \Lambda_G \mathbf{F}$ . It follows that the  $\mathbf{a}$ -update can be computed quickly by using 3D FFT and IFFT:

$$\mathbf{a}^{(k+1)} = \alpha N \mathbf{F}^\dagger \Lambda_G^{-1} \mathbf{F} (\Delta_\Phi^\dagger \mathbf{F}^\dagger \mathbf{S}^t \Delta_\Psi^\dagger \boldsymbol{\sigma} + \mathbf{t}^{(k)}) \quad (12)$$

Note that  $\Delta_\Phi^\dagger \mathbf{F}^\dagger \mathbf{S}^t \Delta_\Psi^\dagger \boldsymbol{\sigma}$  is the PFA map and can be precomputed.

In the end, let us stress that the non-quadratic, non-differentiable and constraint problem (7) can be solved very efficiently with our method by using the ADMM with explicit and separable updates and 3D FFT and IFFT.

#### IV. APPLICATIONS TO REAL DATA

##### A. Spherical measurement setup

The method is evaluated on real measurements from the spherical setup of **Fig. 2**. The microwave instrumentation is made up of two bipolarization monostatic radio frequency (RF) transmitting and receiving antennas, a wideband standard gain horn equipped with a lens, that are driven by a fast network analyzer. See [8] for further details.

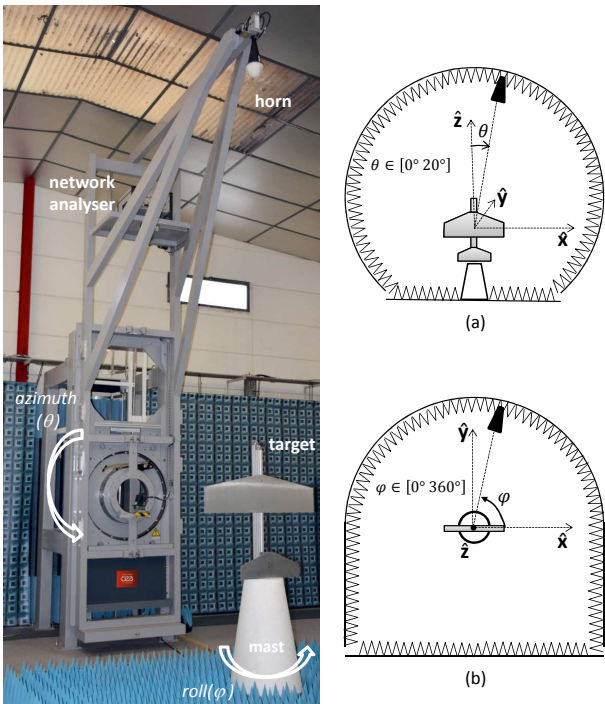


Figure 2: Spherical measurement setup.

The measurement procedure consists of successive steps. Firstly, a calibration by substitution [16] is performed with a standard target (300 mm diameter PEC metallic sphere) whose RCS is computed by Mie series. Secondly, a background subtraction [16] is operated in order to eliminate the background echoes. It is commonly used when the clutter is higher than the target under test. Finally, an adaptive range filter is applied to remove the residual stray echoes that could affect the useful signal (e.g. interactions with walls and floor). Scattering measurements are made for wave frequencies varying from 8 GHz to 12 GHz with increments of 3.9 MHz and angle variation  $\theta = [-20^\circ : 1^\circ : 20^\circ]$  and  $\varphi = [-20^\circ : 4^\circ : 20^\circ]$ .

##### B. Metallic cone with patches

The target is a metallic Perfectly Electrically Conducting (PEC) right circular cone [25] (height: 598.47 mm,

base diameter: 149.33 mm, aperture:  $14.22^\circ$ ) of **Fig. 3**, where 3 metallic rounded patches have been glued to points ②  $z = 115$  mm ( $270^\circ$  roll), ③  $z = 250$  mm ( $-45^\circ$  roll) and ④  $z = 400$  mm ( $135^\circ$  roll). As schematized in **Fig. 3**, it is located on a PMMA supporting mast (dielectric constant  $\epsilon_r = 2.65$ , height: 992 mm, diameter: 40 mm). RCS measurements are made in HH polarization.

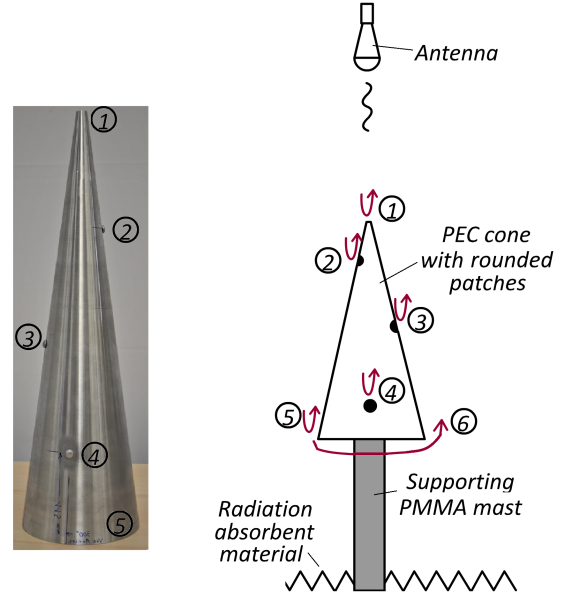


Figure 3: PEC cone (left) and backscattered echoes (right).

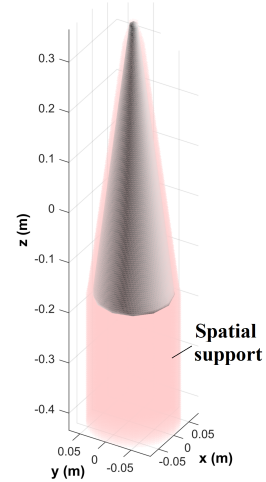


Figure 4: Spatial support constraint.

The RCS map is computed on a grid with  $N \approx 1.7 \cdot 10^7$  voxels ( $N_x \times N_y \times N_z = 256 \times 256 \times 256$ ). A spatial support constraint is defined around and behind the object as illustrated in **Fig. 4**. In the **Fig. 5**, the proposed approach SPRITE is compared to the conventional PFA method and to  $\ell_1$  norm regularization method [9]–[12]. The regularization parameters are manually tuned:  $\mu = 5$ ,  $\lambda = 10$ ,  $\nu = 100$ . The convergence time is 6min 16sec (MATLAB 2013b, Intel Xeon E5-2620 v3 2.4 GHz, 32 Go RAM).

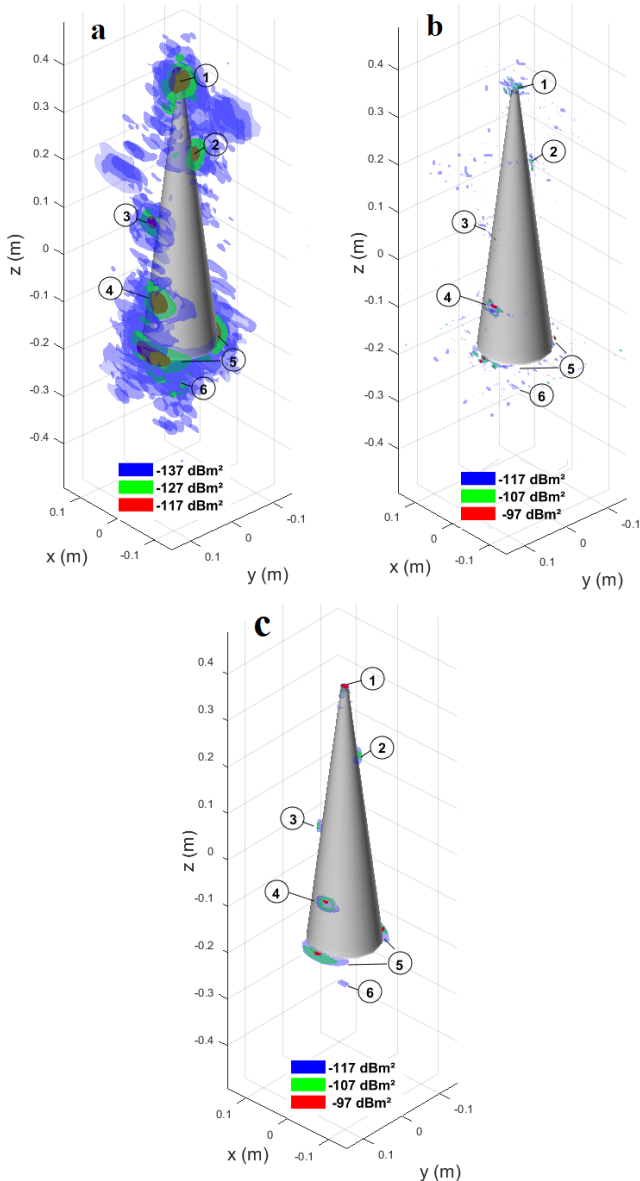


Figure 5: 3D RCS estimated maps with :  
a) PFA – b)  $\ell_1$  norm regularization [9]–[12] – c) SPRITE.  
For a better RCS analysis purpose the target shape is displayed.

In comparison to the PFA map **Fig. 5 a)**, the resolution is drastically increased with the proposed SPRITE method **Fig. 5 c)**. The main scatterers are perfectly located. As illustrated in **Fig. 3**, they come from the diffraction with the tip ①, each metallic patch ②, ③ and ④ and the rear edge ⑤. Behind the object, the SPRITE method exhibits a scatterer ⑥ located at a distance of 87.6 mm from the cone base and that does not appear with the conventional method. After investigations, including RCS computations with a harmonic Maxwell solver [26], this scatterer turns out to originate from the interaction between the creeping wave and the supporting mast. Its location can be explained by the propagation delay inside the PMMA. Moreover, it can be noticed that with the  $\ell_1$  regularization method **Fig. 5 b)** the map is only made up

of scattering points. Conversely, the map obtained with the SPRITE method is not only composed of scattering points but also of specular facets. This better represents the physical reality of scattering mechanisms.

### C. Multistage launcher

The target is the 1.3m height PEC multistage launcher of **Fig. 6**, with a slot located at 67cm from the top and a 2cm diameter flat surface at 14cm. RCS measurements are made in VV polarization. The RCS map is computed on a grid with  $N \approx 3.4 \cdot 10^7$  voxels ( $N_x \times N_y \times N_z = 256 \times 256 \times 512$ ). In the **Fig. 7**, the proposed approach SPRITE is again compared to the conventional PFA method. The regularization parameters are manually tuned:  $\mu = 5$ ,  $\lambda = 15$ ,  $\nu = 50$ .

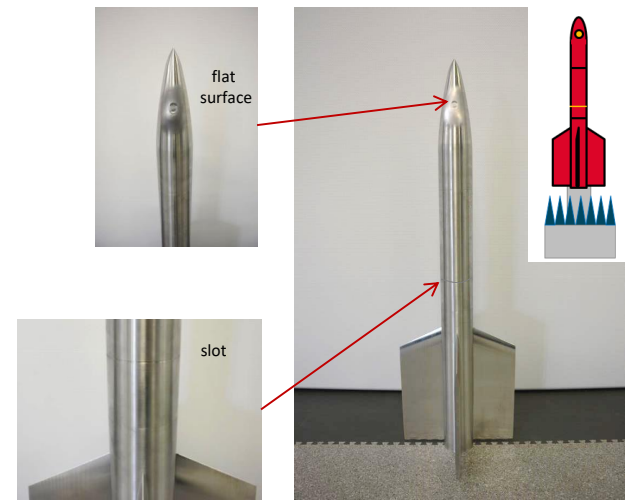


Figure 6: Mx14 multistage launcher.

Once again, the resolution is drastically increased. Contrary to the PFA method, the main scatterers are clearly identified by the SPRITE method and it is possible to distinguish both the slot and the flat surface. Note that a specular echo is exhibited at the bottom of the map; it corresponds to the reflexion with the supporting mast in polystyrene.

## V. CONCLUSION

In this paper, we proposed a new method named SPRITE for 3D HR RCS imaging. The available information on the wave-object interactions lead to different priors and then to a criterion. The RCS map is then defined as the solution of an optimization problem. The minimization is ensured by an efficient algorithm which rests on an Alternating Direction Method of Multipliers. The updates of the auxiliary variables are direct and separable and the map update is computed very efficiently in the frequency domain by 3D FFT and IFFT.

SPRITE is evaluated on real measurement data. In comparison to the conventional method, the resolution is drastically enhanced. The main scatterers are recovered with increased accuracy, leading to a deeper understanding of the target scattering behavior and finally to a better RCS analysis and control. Moreover, unlike recent  $\ell_1$  based methods, the

SPRITE method allows to reconstruct specular facets leading to a better wave-object interactions representation.

As a perspective, we aim to automatically tune the regularization parameters.

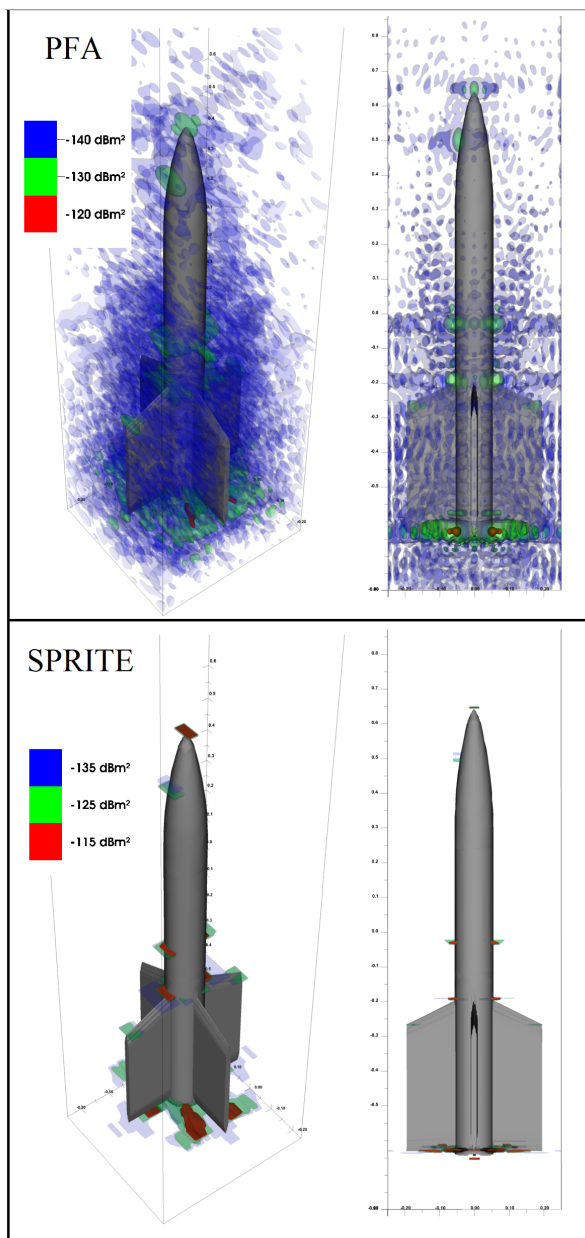


Figure 7: 3D RCS maps, PFA (top) and SPRITE (bottom).

## REFERENCES

- [1] D. L. Mensa, *High Resolution Radar Cross-Section Imaging*, The Artech House radar library. Artech House, Boston, 1981.
- [2] J. Fortuny and A.J. Sieber, "Three-dimensional synthetic aperture radar imaging of a fir tree: first results," *IEEE Transactions on Geoscience and Remote Sensing*, vol. 37, no. 2, pp. 1006–1014, Mar. 1999.
- [3] C. Ozdemir, *Inverse Synthetic Aperture Radar Imaging with MATLAB Algorithms*, Number 210 in Wiley series in microwave and optical engineering. Wiley, Hoboken, NJ, 2012.
- [4] B. Borden, *Radar Imaging of Airborne Targets: a Primer for Applied Mathematicians and Physicists*, Institute of Physics, Bristol ; Philadelphia, 1999.
- [5] M. Cheney and B. Borden, *Fundamentals of Radar Imaging*, Number 79 in CBMS-NSF regional conference series in applied mathematics. Society for Industrial and Applied Mathematics, Philadelphia, 2009.
- [6] T. Benoudiba-Campanini, *Approche Parcimonieuse pour l'Imagerie 3D Haute Résolution de Surface Équivalente Radar*, Ph.D. thesis, University of Bordeaux, 2018.
- [7] J.-F. Giovannelli and J. Idier, *Méthodes d'Inversion Appliquées au Traitement du Signal et de l'Image*, Hermès Science : Lavoisier, Paris, 2013.
- [8] P. Minvielle, P. Massaloux, and J.-F. Giovannelli, "Indoor 3D Radar Imaging for Low-RCS Analysis," *IEEE Transactions on Aerospace and Electronic Systems*, vol. 53, no. 2, pp. 995–1008, Apr. 2017.
- [9] M. Cetin, *Feature-Enhanced Synthetic Aperture Radar Imaging*, Ph.D. thesis, Boston University College of Engineering, 2001.
- [10] L.C. Potter, E. Ertin, J.T. Parker, and M. Cetin, "Sparsity and Compressed Sensing in Radar Imaging," *Proceedings of the IEEE*, vol. 98, no. 6, pp. 1006–1020, June 2010.
- [11] C.D. Austin, E. Ertin, and R.L. Moses, "Sparse Signal Methods for 3D Radar Imaging," *IEEE Journal of Selected Topics in Signal Processing*, vol. 5, no. 3, pp. 408–423, June 2011.
- [12] B. Ji-Hoon, K. Byung-Soo, L. Seong-Hyeon, Y. Eunjung, and K. Kyung-Tae, "Bistatic ISAR image reconstruction using sparse-recovery interpolation of missing data," *IEEE Trans. Aerospace and Electronic Systems*, vol. 52, no. 3, pp. 1155–1167, 2016.
- [13] M. Stuff, M. Biancalana, G. Arnold, and J. Garbarino, "Imaging moving objects in 3D from single aperture synthetic aperture radar," *IEEE NRC*, pp. 94–98, 2004.
- [14] M.L. Burrows, "Two-Dimensional ESPRIT With Tracking for Radar Imaging and Feature Extraction," *IEEE Transactions on Antennas and Propagation*, vol. 52, no. 2, pp. 524–532, Feb. 2004.
- [15] R. Moch, T. Dallmann, and D. Heberling, "A tomographic approach to polarimetric radar cross-section imaging," *IEEE EuCAP*, pp. 3940–3944, Mar. 2017.
- [16] E.F. Knott, J.F. Shaeffer, and M.T. Tuley, *Radar Cross Section*, SciTech radar and defense series. SciTech Pub, Raleigh, NC, 2nd ed., corr. reprinting edition, 2004.
- [17] J.-F. Nouvel, A. Herique, W. Kofman, and A. Safaeinili, "Radar signal simulation: Surface modeling with the Facet Method: Radar Signal Simulation," *Radio Science*, vol. 39, no. 1, Feb. 2004.
- [18] J.-F. Giovannelli and A. Coulais, "Positive deconvolution for superimposed extended source and point sources," *Astronomy & Astrophysics*, vol. 439, no. 1, pp. 401–412, Aug. 2005.
- [19] D.P. Bertsekas, "Nondifferentiable optimization via approximation," in *Nondifferentiable Optimization*, vol. 3, pp. 1–25. Berlin, Heidelberg, 1975.
- [20] B. T. Polyak, *Introduction to Optimization*, Translations series in mathematics and engineering. Optimization Software, Publications Division, New York, 1987.
- [21] P.L. Combettes and V.R. Wajs, "Signal Recovery by Proximal Forward-Backward Splitting," *Multiscale Modeling & Simulation*, vol. 4, no. 4, pp. 1168–1200, Jan. 2005.
- [22] A. Beck and M. Teboulle, "Fast Gradient-Based Algorithms for Constrained Total Variation Image Denoising and Deblurring Problems," *IEEE Transactions on Image Processing*, vol. 18, no. 11, pp. 2419–2434, Nov. 2009.
- [23] S. Boyd, "Distributed Optimization and Statistical Learning via the Alternating Direction Method of Multipliers," *Foundations and Trends in Machine Learning*, vol. 3, no. 1, pp. 1–122, 2010.
- [24] L. Li, X. Wang, and G. Wang, "Alternating Direction Method of Multipliers for Separable Convex Optimization of Real Functions in Complex Variables," *Mathematical Problems in Engineering*, vol. 2015, pp. 1–14, 2015.
- [25] T. Benoudiba-Campanini, P. Minvielle, P. Massaloux, and J.-F. Giovannelli, "A new regularization method for radar cross section imaging," *IEEE EuCAP*, pp. 1419–1423, Mar. 2017.
- [26] B. Stupfel, R. Le Martre, P. Bonnemason, and B. Scheurer, "Combined boundary-element and finite-element method for scattering problem by axi-symmetrical penetrable objects," *Mathematical and numerical aspects of wave propagation phenomena*, pp. 332–341, 1991.